Buoyant flow instability induced by a uniform internal heat source in a vertical annular porous layer

Buoyant flow instability induced by a uniform internal heat source in a vertical annular porous layer

A. Barletta*

Department of Industrial Engineering, Alma Mater Studiorum Università di Bologna, Viale Risorgimento 2, 40136 Bologna, Italy

D.A.S. Rees

Department of Mechanical Engineering, University of Bath, Claverton Down, Bath BA2 7AY, United Kingdom

B. Pulvirenti

Department of Industrial Engineering, Alma Mater Studiorum Università di Bologna, Viale Risorgimento 2, 40136 Bologna, Italy

Abstract

The buoyancy–induced parallel flow in a vertical cylindrical porous layer with annular cross–section is analysed. A radial thermal gradient caused by a uniformly distributed heat source is assumed to induce the buoyant flow. The layer boundaries are modelled as isothermal and permeable to an external fluid reservoir. The onset of the convective instability is analysed by linearising the governing equations for the perturbations. The governing parameters driving the instability are the heat–source Rayleigh number and the ratio between the internal radius and the external radius. Neutral stability curves and the critical values of the Rayleigh number, the perturbation wave number and the angular frequency are computed numerically. It is shown that axisymmetric modes form the most dangerous type of instability.

Keywords: Porous medium, Linear stability, Natural Convection, Normal modes, Internal heating, Cylindrical layer, Vertical buoyant flow

Nomenclature

a	dimensionless parameter, equation (6)
$\hat{\mathbf{e}}_z$	unit vector along the z axis

*Corresponding author

Email addresses: antonio.barletta@unibo.it (A. Barletta), ensdasr@bath.ac.uk (D.A.S. Rees), beatrice.pulvirenti@unibo.it (B. Pulvirenti)

$F(r)$	function, equation (7)
f_n, h_n	eigenfunctions, equation (15)
g	modulus of $\mathbf{g}$
$\mathbf{g}$	gravitational acceleration
H	complex parameter, equation (17)
k	wave number, equation (15)
K	permeability
L_ϕ	dimensionless arc length of a cell
n	integer
p	difference between the pressure and the hydrostatic pressure
P	pressure perturbation, equation (11)
P_n	Fourier coefficient, equation (13)
$\dot{q}$	power per unit volume of the internal heat source
r	radial coordinate
r_1, r_2	internal, external radius
R	Rayleigh number, equation (3)
$\hat{R}, \hat{k}, \hat{\Omega}$	modified parameters, equation (19)
t	time
T	temperature
$\bar{T}$	average temperature
T_s	boundary temperature
$\mathbf{u}$	velocity
u, v, w	r, ϕ, z velocity components
$\bar{w}_b$	average vertical velocity in the basic flow
z	vertical axial coordinate

Greek Symbols

α	average thermal diffusivity
β	thermal expansion coefficient of the fluid
γ	aspect ratio, equation (6)
ε	perturbation parameter, equation (11)
η	complex growth rate, equation (15)
θ	temperature perturbation, equation (11)
θ_n	Fourier coefficient, equation (13)
λ	average thermal conductivity
μ	dynamic viscosity

ξ	real part of η
ρ	reference fluid density
σ	heat capacity ratio
ϕ	angular coordinate
ψ	perturbation streamfunction
ω	imaginary part of $-\eta$
Ω	real parameter, equation (18)

Superscripts, subscripts

b	basic solution, equation (7)
c	critical values

1. Introduction

The onset of thermal instability in a fluid–saturated porous medium has a widespread interest in the heat transfer community, as may be inferred from the quite abundant literature on this topic; see Nield and Bejan [1]. There are several areas of engineering and physics within which such investigations are applied. We just mention the analysis of contaminant diffusion in the soil, the extraction of hydrocarbons, the CO_2 sequestration processes, and the use of metal foams for the optimised design of heat exchangers. If most of the studies published in the last decades are focussed on the thermal instability of the Rayleigh–Bénard type, where the fluid is initially at rest while experiencing a purely conductive heat transfer, there are other analyses devoted to side heating conditions or internal heating conditions in vertical porous layers, where a stationary and parallel buoyant flow may give rise to a multi–cellular instability pattern. A survey of the latter type of instability may be found in Chapter 7 of Nield and Bejan [1]. Recent important results have been discussed by several authors [2–8]. In particular, Barletta and Celli [6] proved that the parallel buoyant flow in a plane vertical porous layer with a uniform internal heat source may become unstable even in the absence of a temperature difference between the boundaries.

The aim of this paper is to develop and extend the stability analysis presented in Barletta and Celli [6] by investigating the effect of curvature when a vertical annular porous layer is considered instead of a plane vertical layer. The plane layer behaviour of Barletta and Celli [6] is then found as a limiting case where the aspect ratio between the internal radius and the external radius of the annulus tends to unity. The present stability analysis is carried out by assuming small–amplitude perturbations of the basic buoyant flow. The linear dynamics of perturbations is determined by employing a modal analysis. The resulting eigenvalue problem is solved numerically, thus providing the neutral stability curves and the critical values for the onset of the instability as a function of

the aspect ratio of the annulus.

2. Mathematical model

By analogy with the system studied by Barletta and Celli [6], we consider a vertical porous annulus with infinite height, internal radius r_1 and external radius r_2. A fluid saturates the porous medium. Cylindrical coordinates (r, ϕ, z) are chosen so that the vertical coordinate, z, is also the axis of the cylinder. A uniform internal heat source, with power per unit volume $\dot{q}$, is present inside the annulus. We can devise conditions such that $\dot{q}$ is caused by the Joule heating due to a stationary electric current in the porous medium or, alternatively, caused by an exothermic chemical reaction. The boundaries $r = r_1$ and $r = r_2$ are considered to be both isothermal and permeable, with a uniform temperature, T_s, and the pressure equal to the hydrostatic pressure of the fluid. The latter condition models perfect permeability of the boundary to an external fluid reservoir at rest. By introducing the local difference between the pressure and the hydrostatic pressure, p, the boundary conditions are that $p = 0$ at both $r = r_1$ and $r = r_2$. A sketch of the porous layer and of the boundary conditions is shown in Fig. 1.

2.1. Governing equations

The governing equations for the seepage flow in the porous cylinder are based on the Oberbeck–Boussinesq approximation and on Darcy's law [1]. Hence, we write

$$\boldsymbol{\nabla} \cdot \mathbf{u} = 0, \tag{1a}$$

$$\frac{\mu}{K}\,\mathbf{u} = -\,\boldsymbol{\nabla} p + \rho g \beta \big(T - \bar{T}\big)\hat{\mathbf{e}}_z, \tag{1b}$$

$$\sigma \frac{\partial T}{\partial t} + \mathbf{u} \cdot \boldsymbol{\nabla} T = \alpha \left(\nabla^2 T + \frac{\dot{q}}{\lambda} \right), \tag{1c}$$

which express the local mass balance equation (1a), the local momentum balance equation (1b) and the heat transport equation (1c). In equations (1), $\mathbf{u}$ is the seepage velocity with components (u, v, w) along the (r, ϕ, z) directions, T is the temperature field and t is the time. Furthermore, in equations (1), μ, β and ρ are the fluid dynamic viscosity, thermal expansion coefficient and reference density, while α is the average thermal diffusivity of the saturated medium, λ is the average thermal conductivity of the saturated porous medium, K its permeability and σ the ratio between the volumetric heat capacity of the saturated porous medium and that of the fluid. Here, the volumetric heat capacity means the product between the density and the specific heat. When we consider the volumetric heat capacity of the saturated porous medium, this is intended as the weighted average between the solid and the fluid. We also note that the average thermal diffusivity α is defined as the ratio between the average thermal conductivity λ and the volumetric heat

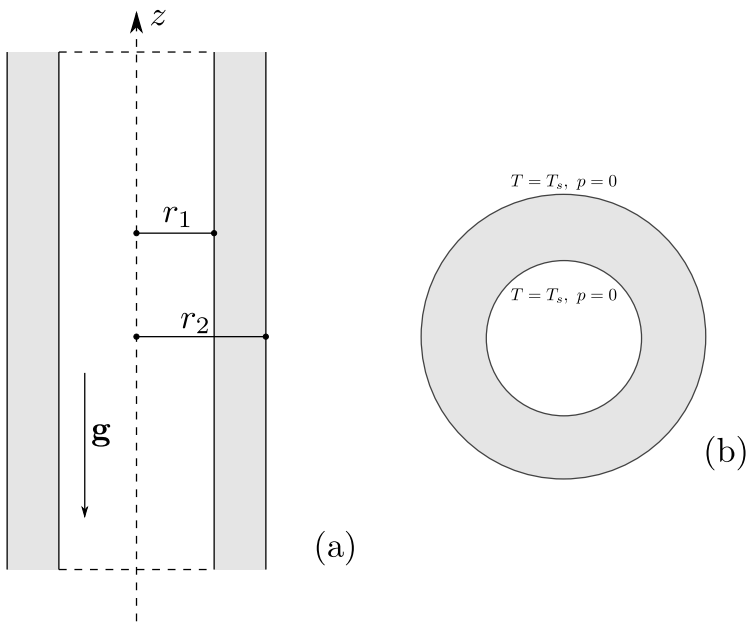

Figure 1: A sketch of the cylindrical porous layer and of the boundary conditions: longitudinal section (a); transverse section (b).

capacity of the fluid. The modulus of the gravitational acceleration is g and $\hat{\mathbf{e}}_z$ is the unit vector along the z axis.

The constant $\bar{T}$ denotes the average temperature in an annular cross–section ($z = constant$) evaluated for the basic state to be defined in the forthcoming Section 2.4. The local balance equations (1) can be rewritten in a dimensionless form by means of the scaling

$$\frac{1}{r_2}\,(r,z) \to (r,z), \quad \frac{\alpha}{\sigma r_2^2}\,t \to t, \quad \frac{K}{\mu\alpha}\,p \to p,$$
$$\frac{r_2}{\alpha}\,\mathbf{u} = \frac{r_2}{\alpha}\,(u,v,w) \to (u,v,w) = \mathbf{u}, \quad \lambda\,\frac{T-\bar{T}}{\dot{q}r_2^2} \to T. \tag{2}$$

The Rayleigh number R is defined as

$$R = \frac{\rho g \beta \dot{q} K r_2^3}{\lambda \mu \alpha}, \tag{3}$$

using the outer radius, r_2, as the length scale. From equations (1)–(3), we obtain

$$\boldsymbol{\nabla}\cdot\mathbf{u} = 0, \tag{4a}$$
$$\mathbf{u} = -\,\boldsymbol{\nabla}p + R\,T\,\hat{\mathbf{e}}_z, \tag{4b}$$
$$\frac{\partial T}{\partial t} + \mathbf{u}\cdot\boldsymbol{\nabla}T = \nabla^2 T + 1. \tag{4c}$$

We mention that the dimensional average temperature $\bar{T}$ defines the reference temperature within the Oberbeck–Boussinesq approximation. Thus, when either $T = \bar{T}$ (by using dimensional temperatures) or $T = 0$ (by using the dimensionless temperature), the buoyancy force is zero.

2.2. Experimental support for the mathematical model

The above described mathematical model is based on two important features:

(a) The combined use of the Oberbeck–Boussinesq approximation and of Darcy's law as a framework for modelling convection in porous media;

(b) A uniform internal heat source acting in a solid material as a cause of buoyant fluid flow.

Regarding feature (a), there are several experimental studies supporting Darcy's law as suitably modified to include the buoyancy force. Indeed, the classical Oberbeck–Boussinesq scheme is adapted to fluid saturated porous media. We refer the readers to Nield and Bejan [1] for a survey of the experiments supporting the Oberbeck–Boussinesq scheme when the fluid seepage in the porous medium satisfies Darcy's law. The analysis of the experiments on the convective flows in porous media reported in this book is primarily significant for the present study when it is focussed on the onset of cellular convection patterns as induced by thermal instability in a fluid saturated porous medium. Chapter 6 of Nield and Bejan [1] is devoted to this subject. The cornerstone paper by Hartline and Lister [9] deserves a special attention. In fact, the authors provide experimental support for the emergence of the Rayleigh–Bénard instability in a fluid saturated porous medium. Such experimental evidence was further discussed in Lister [10], where multiple data sets obtained in different experimental studies were compared. The conclusions drawn by Hartline and Lister [9] and by Lister [10] show clearly that the theoretical studies presented in the classical papers on the thermal instability in porous media by Horton and Rogers [11] and by Lapwood [12] are in excellent agreement with experiments. We mention that Lister [10] performed two experiments on water convection in either a rubberized curled coconut fibre layer or in a a polymethylmethacrylate beads layer. Such experiments not only support the theoretical predictions for the critical Rayleigh number at onset of thermal instability, but also the heat transfer rates numerically evaluated for the supercritical regime.

The natural convection flow from internal heat sources in a solid material is the ground of feature (b). The pioneering paper by Smith and Hammitt [13] presents a comparison between numerical and experimental results for the buoyant flow in a rectangular cavity with internal heat generation. The internal heating is due to an electric power supplied within the cavity, while the fluid employed in the experimental setup is water. The study by Bhowmik and Tou [14] provides an interesting account of transient natural convection heat transfer from an array of electronic chips. The authors discuss an experiment on the power–on unsteady natural convection heat transfer caused by a linear array of discrete heat sources in a rectangular channel where the liquid coolant is water with Prandtl number 5.5. Lee et al. [15] present an experiment where they simulate how the thermal load from the decay of heat-generating debris causes a natural convection response in a fluid vessel during a severe nuclear reactor accident. The method employed by these authors

to obtain the internal heating is by the Joule effect due to an alternating electric current in an internal solid heater within the vessel filled with water. They also demonstrated the feasibility of their method in order to simulate a uniform volumetric heat source.

2.3. Boundary conditions

In dimensionless form, the pressure and temperature boundary conditions are expressed as

$$p = 0, \quad T = a \quad \text{at} \quad r = \gamma \quad \text{and} \quad r = 1, \tag{5}$$

where γ is the aspect ratio and a is a dimensionless parameter given by

$$\gamma = \frac{r_1}{r_2}, \quad a = \lambda \, \frac{T_s - \bar{T}}{\dot{q} r_2^2}. \tag{6}$$

As it will become clearer in the next Section 2.4, the value of a depends on the net flow rate across the porous annulus.

2.4. Basic buoyant flow

A steady and axisymmetric parallel flow in the vertical z direction exists. It is defined by the solution of equations (4) and (5) and expressed as

$$\begin{aligned} &u_b = 0 = v_b, \quad w_b(r) = R\,[a + F(r)], \\ &T_b(r) = a + F(r), \quad p_b = 0, \quad \text{with} \quad F(r) = \frac{\left(1 - r^2\right)\ln(\gamma) - \left(1 - \gamma^2\right)\ln(r)}{4\ln(\gamma)}. \end{aligned} \tag{7}$$

Here, the subscript "b" serves to denote the "basic" flow. The flow is caused entirely by the buoyancy force as may easily be inferred from the velocity being proportional to the Rayleigh number R. The value of the parameter a is correlated to the flow rate across a z = *constant* cross–section,

$$\bar{w}_b = \frac{2}{1 - \gamma^2} \int_\gamma^1 w_b \, r \, \mathrm{d}r = R \left[a + \frac{1 - \gamma^2 + \left(1 + \gamma^2\right)\ln(\gamma)}{8\ln(\gamma)} \right]. \tag{8}$$

There exists a special case,

$$a = -\frac{1 - \gamma^2 + \left(1 + \gamma^2\right)\ln(\gamma)}{8\ln(\gamma)}, \tag{9}$$

which defines a condition of zero flow rate in the basic state. Such a condition corresponds to when the fluid is confined within an annulus which is very considerably taller than its outer radius. We point out that equations (6) and (9) implicitly define the constant reference temperature $\bar{T}$ employed in equation (1b).

We mention that the basic flow defined by equation (7) entails a uniform distribution of p_b, throughout the annular region $1 < r < \gamma$, with $p_b = 0$ everywhere. This yields both $p_b = 0$ and $\partial p_b/\partial r = 0$ for the whole region $1 < r < \gamma$. The feature of the basic flow $\partial p_b/\partial r = 0$ is consistent with $u_b = 0$, which is a consequence of equation (4b) and which is also evidenced in equation (7). Then, we have $u_b = 0$ for the whole region $1 < r < \gamma$. As a consequence, one can infer that $u_b = 0$ at the boundaries, *i.e.*, for $r \to 1$ and for $r \to \gamma$. One can correctly say that for the basic flow, and only for the basic flow, the boundaries satisfy simultaneously the constraints $p_b = 0$ and $u_b = 0$. The latter condition describes absence of flow across the boundaries $r = 1$ and $r = \gamma$, or impermeability of such boundaries, which is a logical consequence of having assumed a purely vertical basic flow. However, the boundary conditions for the basic flow and for the perturbed flow, to be discussed in Section 3, are those specified by equation (5) constraining the boundaries to be permeable with $p = 0$.

2.5. Pressure–temperature formulation

By evaluating the divergence of equation (4b) and by employing equation (4a), we can rewrite equations (4) and (5) as

$$\nabla^2 p = R\,\frac{\partial T}{\partial z}, \tag{10a}$$

$$\frac{\partial T}{\partial t} - \boldsymbol{\nabla} p \cdot \boldsymbol{\nabla} T + R\,T\,\frac{\partial T}{\partial z} = \nabla^2 T + 1, \tag{10b}$$

$$p = 0, \quad T = a \quad \text{at} \quad r = \gamma, 1. \tag{10c}$$

The advantage in the formulation (10) relies on the reduced number of unknowns (p, T) to be determined with respect to equations (4), where the unknowns are $(\mathbf{u}, p, T)$.

3. Linear stability analysis

It is well-known that stationary solutions of the governing equations might be unstable under certain parametric conditions. In our case, the basic flow (7) may be stable or unstable depending on the parameters γ and R. By introducing the perturbation parameter ε, where $|\varepsilon| \ll 1$ is assumed, we will carry out a linear stability analysis of the perturbations superposed onto the basic flow (7). Hence, by employing equation (7), we write

$$p(r, \phi, z, t) = \varepsilon P(r, \phi, z, t), \quad T(r, \phi, z, t) = a + F(r) + \varepsilon\theta(r, \phi, z, t), \tag{11}$$

where (P, θ) are the perturbations. If we substitute equation (11) into equations (10) and if we neglect terms of $O(\varepsilon^2)$, then we obtain the linearised governing equations for the unknowns (P, θ),

namely

$$\nabla^2 P = R\,\frac{\partial \theta}{\partial z}, \tag{12a}$$

$$\frac{\partial \theta}{\partial t} - F'(r)\,\frac{\partial P}{\partial r} + R\,[a + F(r)]\,\frac{\partial \theta}{\partial z} = \nabla^2 \theta, \tag{12b}$$

$$P = 0, \quad \theta = 0 \quad \text{at} \quad r = \gamma, 1, \tag{12c}$$

where primes serve to denote derivatives with respect to r. The dependence on the angular coordinate ϕ can be managed by using the Fourier series,

$$P(r,\phi,z,t) = \sum_{n=0}^{\infty} P_n(r,z,t)\cos(n\phi),$$

$$\theta(r,\phi,z,t) = \sum_{n=0}^{\infty} \theta_n(r,z,t)\cos(n\phi). \tag{13}$$

Thus, we obtain for $n = 0, 1, 2, \ldots$

$$\frac{1}{r}\,\frac{\partial}{\partial r}\left(r\,\frac{\partial P_n}{\partial r}\right) + \frac{\partial^2 P_n}{\partial z^2} - \frac{n^2}{r^2} P_n = R\,\frac{\partial \theta_n}{\partial z}, \tag{14a}$$

$$\frac{1}{r}\,\frac{\partial}{\partial r}\left(r\,\frac{\partial \theta_n}{\partial r}\right) + \frac{\partial^2 \theta_n}{\partial z^2} - \frac{n^2}{r^2}\theta_n = \frac{\partial \theta_n}{\partial t} - F'(r)\,\frac{\partial P_n}{\partial r} + R\,[a + F(r)]\,\frac{\partial \theta_n}{\partial z}, \tag{14b}$$

$$P_n = 0, \quad \theta_n = 0 \quad \text{at} \quad r = \gamma, 1. \tag{14c}$$

We now focus on the dynamics of normal modes expressed as

$$P_n(r,z,t) = f_n(r)\,e^{\eta t}\,e^{ikz}, \quad \theta_n(r,z,t) = h_n(r)\,e^{\eta t}\,e^{ikz}, \tag{15}$$

with a real wave number, k, and the complex growth rate, η. The substitution of equation (15) into equation (14) yields

$$f_n'' + \frac{1}{r}\,f_n' - \left(\frac{n^2}{r^2} + k^2\right) f_n - ikR\,h_n = 0, \tag{16a}$$

$$h_n'' + \frac{1}{r}\,h_n' - \left[\frac{n^2}{r^2} + k^2 + H + ikR\,F(r)\right] h_n + F'(r)\,f_n' = 0, \tag{16b}$$

$$f_n = 0, \quad h_n = 0 \quad \text{at} \quad r = \gamma, 1, \tag{16c}$$

where we defined the modified complex parameter H as

$$H = \eta + iakR. \tag{17}$$

The real part of H coincides with the real part of η and, hence, with the growth rate of the normal mode. If we denote with $\xi = \mathrm{Re}(H) = \mathrm{Re}(\eta)$ the exponential growth rate, then $\xi > 0$ defines

instability, $\xi < 0$ stability and $\xi = 0$ neutral stability. The imaginary part of η is equal to $-\omega$, where ω is the angular frequency of the normal mode. We can denote the imaginary part of H as $-\Omega$. Thus, by employing equation (17), we can write

$$\Omega = \omega - akR. \tag{18}$$

Equations (16) form a system of homogeneous ordinary differential equations with homogeneous boundary conditions. In fact, equations (16) yield an eigenvalue problem where the eigenfunctions (f_n, h_n) are to be numerically computed together with the complex eigenvalue H, for every prescribed input parameters (n, k, R). As a consequence of the definition (17), the parameter a is not involved explicitly in the solution of the eigenvalue problem. In particular, this means that the eigenvalue H is independent of a.

The numerical solution of equations (16) as a differential eigenvalue problem is performed via the shooting method using an adaptive grid. We omit here the details of this procedure which is described in Chapter 9 of the book by Straughan [16] and in Chapter 10 of the book by Barletta [17] where details about the coding of the numerical solver are also provided. The minimum of the neutral curve is obtained by means of an extended system as described in Barletta [17]. Numerical data quoted below are accurate to six significant figures.

4. Discussion of the results

The onset of the convective instability is identified by the neutral stability curve, defined as the locus in the (k, R) plane where $\xi = \mathrm{Re}(H) = 0$. However, since the comparison with the instability observed in the case of a vertical plane layer is important, it is quite convenient to rescale the pertinent parameters governing the transition to instability,

$$\hat{R} = (1-\gamma)^3 R, \quad \hat{k} = (1-\gamma)k, \quad \hat{\Omega} = (1-\gamma)^2 \Omega. \tag{19}$$

Such a rescaling is motivated by the change of the reference length from r_2, employed in equation (2), to the thickness $r_2 - r_1$, which is the equivalent of the natural reference length for a plane layer [6]. By adopting the rescaled parameters defined by equation (19), the results for the plane layer are retrieved through the asymptotic solution for $\gamma \to 1$. We recall that, according to Barletta and Celli [6], the asymptotic case $\gamma \to 1$ features

$$\hat{R}_c = 740.027, \quad \hat{k}_c = 1.94671, \quad \hat{\Omega}_c = 197.192, \tag{20}$$

where the subscript "c" denotes the "critical" condition, namely the minimum R position along the neutral stability curve drawn in the (k, R) plane, for a given γ.

γ	n	$\hat{R}_c$	$\hat{k}_c$	$\hat{\Omega}_c$
0.99	0	740.026	1.94671	197.192
	1	740.035	1.94671	197.194
	2	740.065	1.94670	197.201
	3	740.114	1.94669	197.211
0.75	0	738.909	1.94545	197.228
	1	747.021	1.94396	198.914
	2	771.981	1.93864	204.022
	3	815.831	1.92691	212.704
0.5	0	734.050	1.93913	197.448
	1	782.121	1.92855	207.350
	2	952.123	1.86815	238.931
	3	1388.49	1.65609	300.100
0.25	0	722.518	1.91299	198.827
	1	935.255	1.84584	240.859
	2	3212.34	1.03842	440.713

Table 2: Critical values of $\hat{R}$, $\hat{k}$ and $\hat{\Omega}$, for some values of γ and n.

Table 2 reports some values of $(\hat{R}_c, \hat{k}_c, \hat{\Omega}_c)$ versus γ and n. The general evidence is that the dependence on n is very weak when the annulus has a small curvature ($\gamma = 0.99$) even if, also in this case, $\hat{R}_c$ increases with n. On the other hand, the dependence on n becomes more and more dramatic as γ decreases. This phenomenon is apparent especially with regard to the values of $\hat{R}_c$. In the case $\gamma = 0.25$, reported in Table 2, the critical values for $n = 3$ could not be computed and, hence, they are omitted in the table. A possible reason is that, with $\gamma = 0.25$ and $n = 3$, the value of $\hat{R}_c$ becomes so large that numerical accuracy is lost. Moreover, Table 2 shows that the critical values for $\gamma = 0.99$ and $n = 0$ coincide to within six significant figures with the asymptotic values obtained by Barletta and Celli [6] and reported above in equation (20). Table 2 suggests that the smallest value of $\hat{R}_c$ corresponds to when $n = 0$ (axisymmetric modes) and that it decreases with γ. Thus, a departure from the plane layer geometry by having an increased curvature of the annulus causes the basic flow to be destabilised at decreasing values of $\hat{R}_c$.

Figure 2 illustrates how $\hat{R}_c$ varies with γ for $n = 0, 1, 2, 3$. As has already been commented on when discussing the data in Table 2, the modes with $n = 0$ are those which trigger the instability at the smallest value of $\hat{R}_c$. The value of $\hat{R}_c$ for $n = 0$ decreases slightly when γ decreases from 1 to $\gamma = 0.146052$, and thereafter $\hat{R}_c$ increases rapidly as γ decreases still further. The minimum

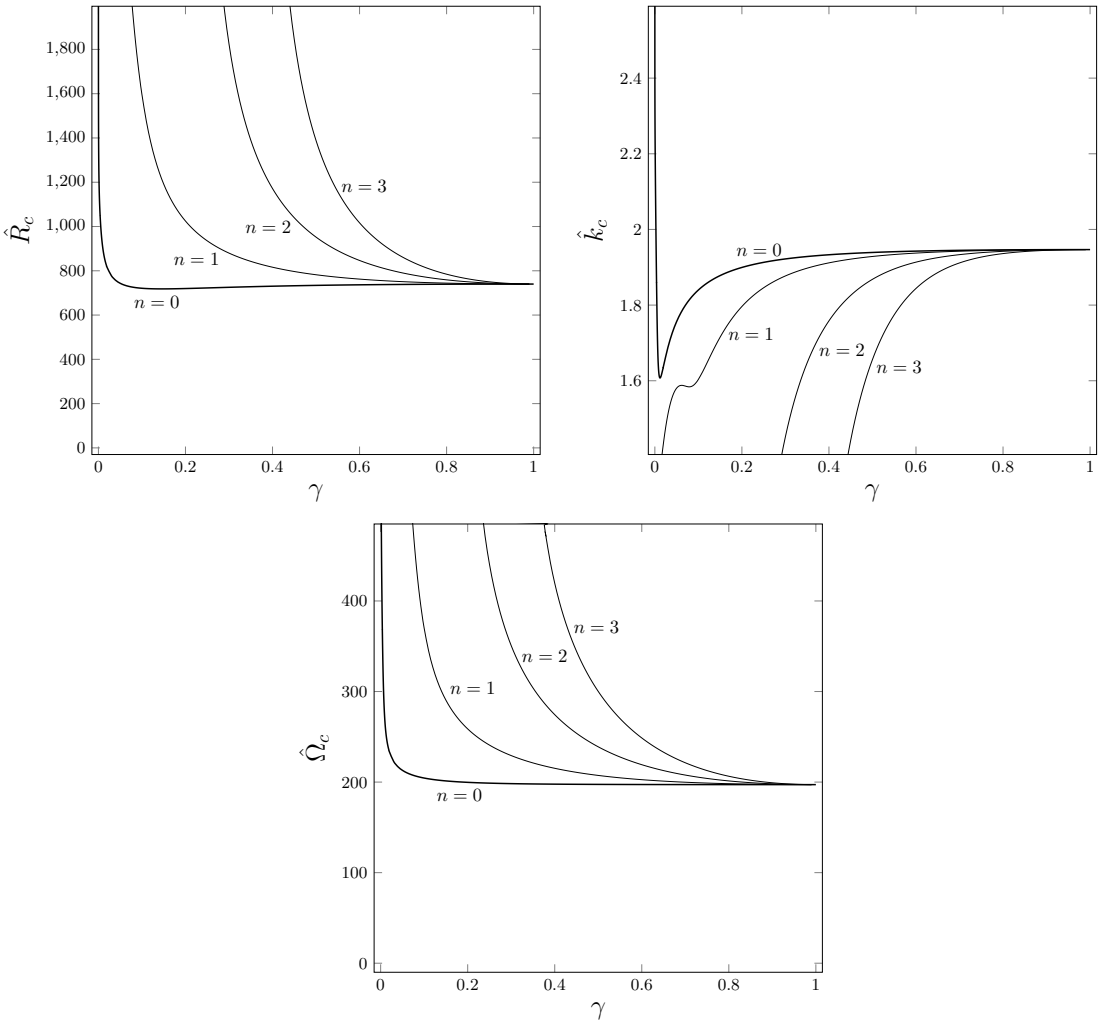

Figure 2: Variation of $\hat{R}_c$, $\hat{k}_c$ and $\hat{\Omega}_c$ wth γ for $n = 0$ (thick line) and for $n = 1, 2, 3$ (thin lines).

value which occurs at $\gamma = 0.146052$ is $\hat{R}_c = 718.208$. Generally, Figure 2 shows that $\hat{k}_c$ decreases and $\hat{\Omega}_c$ increases as γ decreases from 1, although there is an exception in a narrow region with $0 < \gamma < 0.011879$ where $\hat{k}_c$ increases once more as γ decreases. We reckon that, with such small values of γ, the sensitivity to the change of the aspect ratio is mainly due to the boundary conditions at the inner boundary which may turn out to be poorly realistic in the limit $\gamma \to 0$.

The critical values discussed so far result from minimising $\hat{R}$ in the $(\hat{k}, \hat{R})$ plane along the neutral stability curves. Then, Figure 3 displays the neutral stability curves in the $(\hat{k}, \hat{R})$ plane for a few sample aspect ratios, $\gamma = 0.99, 0.75, 0.5, 0.25$, illustrating the effect of a gradual departure from the zero curvature limit, $\gamma \to 1$, analysed by Barletta and Celli [6]. The behaviour is monitored for the modes $n = 0, 1, 2$ as higher values of n yield higher threshold values of $\hat{R}$ for the transition to instability, as already illustrated through Table 2 and Figure 2. As evidenced above, the effect of n

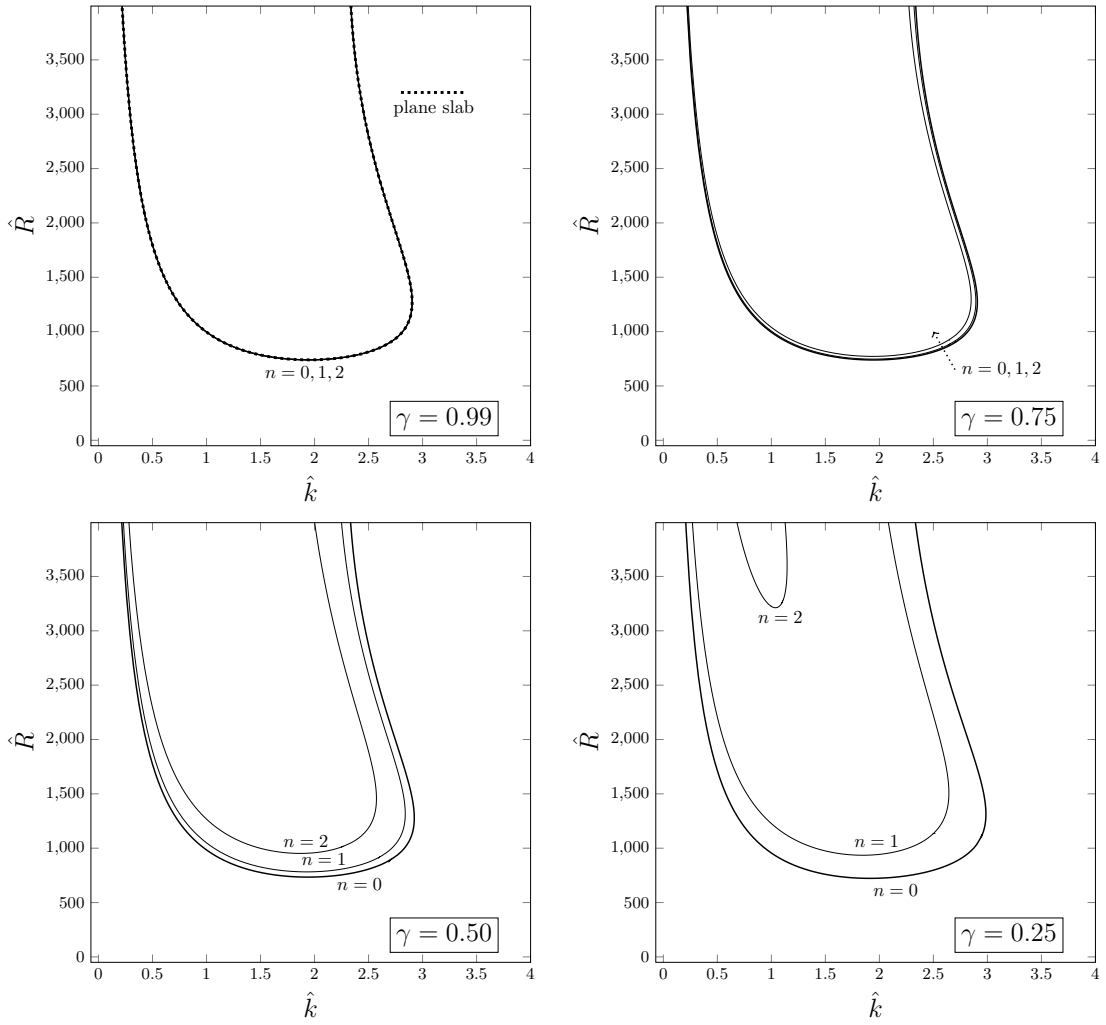

Figure 3: Neutral stability curves in the $(\hat{k}, \hat{R})$ plane for $n = 0$ (thick line) and for $n = 1, 2$ (thin lines). Different frames correspond to different aspect ratios, γ. The dotted line in the frame with $\gamma = 0.99$ corresponds to the data for the plane slab [6].

is extremely small, hardly visible, when γ is close to 1, while this effect is more and more significant as γ decreases. In the frame for $\gamma = 0.99$, the curves with $n = 0, 1, 2$ cannot be distinguished. On the other hand, they are substantially different from one another when $\gamma = 0.25$. For this value of γ, there is a very large difference between the neutral stability curves with $n = 1$ and $n = 2$. This result indicates that, when γ is small, non–axisymmetric modes act in a markedly different way with respect to each other and to the axisymmetric modes, which is not the case for $\gamma \to 1$. Finally, we mention that Figure 3 shows clearly that the data for $\gamma = 0.99$ yield neutral stability curves which are almost indistinguishable from one another, and from the one (dotted curve) reported in Barletta and Celli [6] for the plane slab case, *i.e.* the limit $\gamma \to 1$.

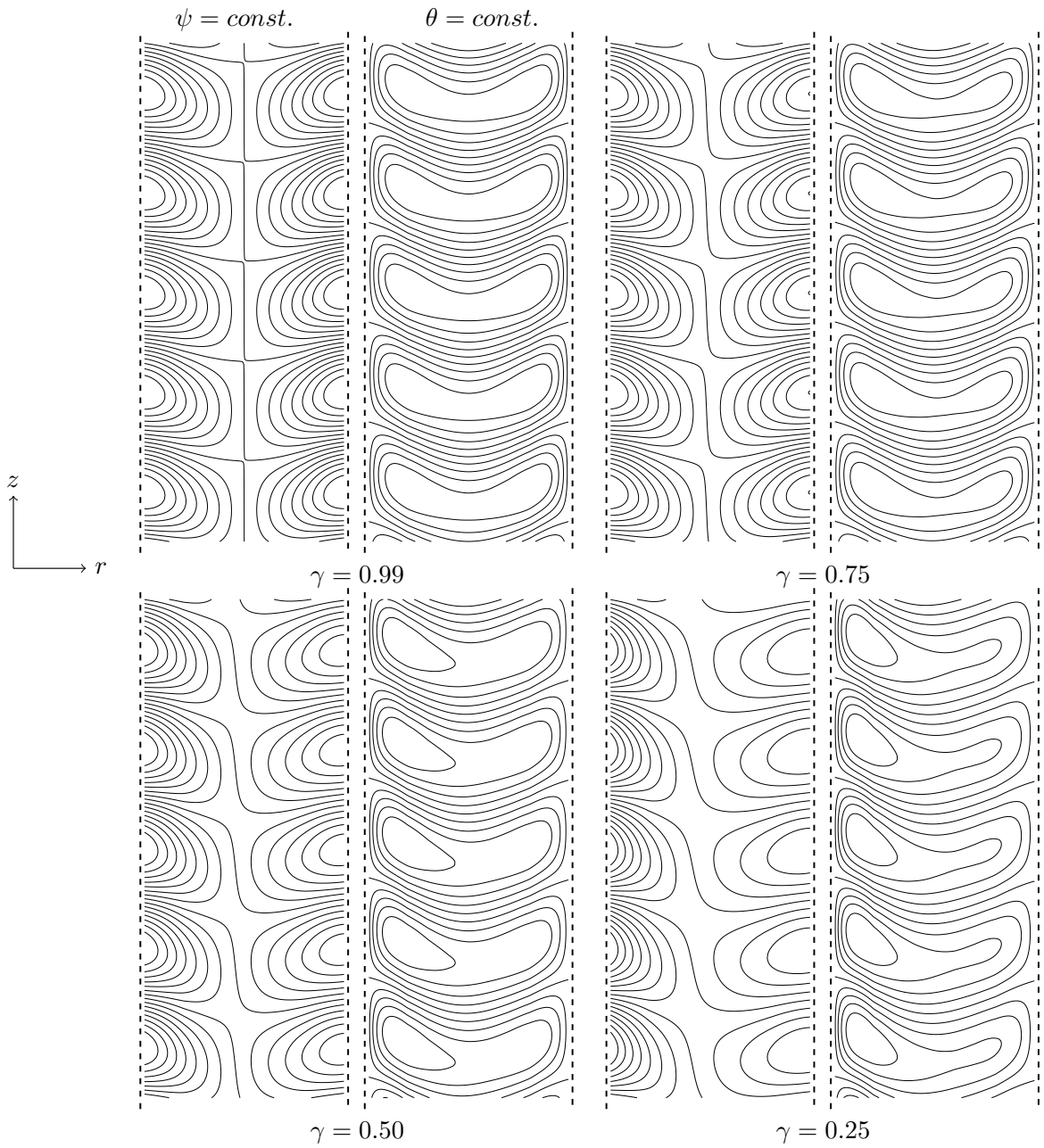

Figure 4: Streamlines ($\psi = constant$) and isotherms ($\theta = constant$) in the (r, z) plane for the axisymmetric perturbation modes ($n = 0$) with critical conditions and different aspect ratios γ.

A physical argument justifying the apparent equivalence of different $n > 0$ modes at onset of instability when γ is very close to unity is as follows. The dimensionless arc length of a cell in the (r, ϕ) plane, L_ϕ, can be evaluated by employing equation (13). It depends on the nonzero value of

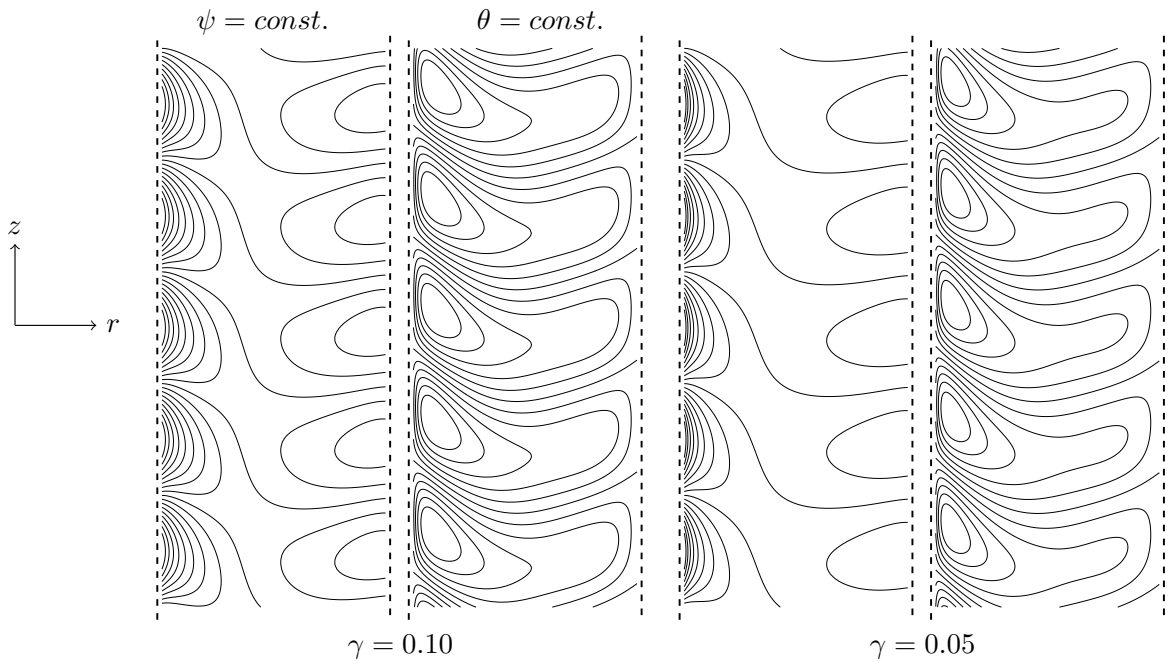

Figure 5: Streamlines ($\psi = constant$) and isotherms ($\theta = constant$) in the (r, z) plane for the axisymmetric perturbation modes ($n = 0$) with critical conditions and different aspect ratios γ.

n and is given by, approximately,

$$L_\phi = \frac{\pi(1+\gamma)}{2n}, \tag{21}$$

where we have assumed the reference radius as the arithmetic mean between the external and internal radii. L_ϕ is to be compared with the radial width of the cell,

$$L_r = 1 - \gamma. \tag{22}$$

If n is such that $L_r \ll L_\phi$, then the non-axisymmetric modes are comparable with the axisymmetric modes in the onset of instability. Thus, in order to see a significantly strong effect of n, one should consider modes with

$$n \sim \frac{\pi(1+\gamma)}{2(1-\gamma)}, \tag{23}$$

or larger. Such n is greater than 10^2 when $\gamma = 0.99$, while it is greater than 10 when $\gamma = 0.75$ and it decreases sensibly with smaller values of γ.

Figure 4 shows the streamlines and isotherms in the (r, z) plane for the axisymmetric perturbation modes under critical conditions, $\hat{R} = \hat{R}_c$, $\hat{k} = \hat{k}_c$ and $\hat{\Omega} = \hat{\Omega}_c$. For the purpose of drawing the streamlines, we defined a suitable streamfunction, ψ, such that

$$\frac{1}{r}\frac{\partial \psi}{\partial z} \quad \text{and} \quad -\frac{1}{r}\frac{\partial \psi}{\partial r}$$

yield the r and z components of the perturbation velocity, respectively. By decreasing gradually γ from 0.99 to 0.25, we test of the effect of an increasing curvature of the layer on the shape of the cellular patterns. We see that we have a substantial symmetry of the cells when $\gamma = 0.99$ which is slightly broken when $\gamma = 0.75$. The asymmetric form of the cells is quite perceivable for $\gamma = 0.5$ and becomes even more pronounced for $\gamma = 0.25$. There is a tendency for the cells to acquire a boundary layer structure close to the internal boundary at $r = \gamma$ as γ decreases. Such a trend is further exploited with very small values of γ, as illustrated in Fig. 5 where the aspect ratios $\gamma = 0.1$ and $\gamma = 0.05$ are considered.

5. Conclusions

The stationary and parallel buoyant flow in a vertical porous layer with an annular cross–section has been studied. A uniform internal heat source drives the buoyant flow, leading to instability when its intensity is sufficiently large. The internal and external cylindrical boundaries have been modelled as permeable and with the same given temperature. The governing parameters driving the transition to convective instability are the Rayleigh number, R, which is proportional to the heat source intensity, and the aspect ratio, γ, between the internal radius and the external radius of the annulus. A linear stability analysis has been carried out for the determination of the neutral stability condition and of the critical Rayleigh number for a wide range of aspect ratios, γ. The main focus has been the evaluation of the effects of the aspect ratio γ on the onset of the instability, by considering the limit $\gamma \to 1$ as the reference condition. Indeed, such a limit corresponds to the case of a plane layer which was examined previously by Barletta and Celli [6]. Thus, gradually decreasing values of γ have revealed the effects of an increasing curvature of the layer. Among the most interesting results obtained from this study we mention the following:

- The most unstable perturbation modes are axisymmetric. The distinction between the onset thresholds of axisymmetric and non–axisymmetric perturbation modes tends to be more and more significant as γ decreases below unity.
- The evaluation of the critical Rayleigh number revealed that an increasing curvature of the layer generally destabilises the basic buoyant flow. An exception to this trend emerges for very small γ, namely a parametric domain where the assumed boundary condition at the internal boundary appears to be difficult to implement in a real–world system.

Acknowledgements

The authors A. Barletta and B. Pulvirenti acknowledge the financial support from the grant PRIN 2017F7KZWS provided by the Italian Ministry of Education and Scientific Research.

References

[1] D. A. Nield, A. Bejan, Convection in Porous Media, Springer, New York, 5th edition, 2017.

[2] D. A. S. Rees, The effect of local thermal nonequilibrium on the stability of convection in a vertical porous channel, Transport in Porous Media 87 (2011) 459–464.

[3] N. L. Scott, B. Straughan, A nonlinear stability analysis of convection in a porous vertical channel including local thermal nonequilibrium, Journal of Mathematical Fluid Mechanics 15 (2013) 171–178.

[4] A. Barletta, A proof that convection in a porous vertical slab may be unstable, Journal of Fluid Mechanics 770 (2015) 273–288.

[5] B. M. Shankar, I. S. Shivakumara, On the stability of natural convection in a porous vertical slab saturated with an Oldroyd–B fluid, Theoretical and Computational Fluid Dynamics 31 (2017) 221–231.

[6] A. Barletta, M. Celli, Instability of parallel buoyant flow in a vertical porous layer with an internal heat source, International Journal of Heat and Mass Transfer 111 (2017) 1063–1070.

[7] S. B. Naveen, B. M. Shankar, I. S. Shivakumara, Finite Darcy–Prandtl number and maximum density effects on Gill's stability problem, Journal of Heat Transfer 142 (2020).

[8] B. M. Shankar, I. S. Shivakumara, S. B. Naveen, Impact of thermal non–equilibrium on the stability of natural convection in an Oldroyd–B fluid–saturated vertical porous layer with internal heat sources, Transport in Porous Media 133 (2020) 437–458.

[9] B. K. Hartline, C. R. B. Lister, Thermal convection in a Hele–Shaw cell, Journal of Fluid Mechanics 79 (1977) 379–389.

[10] C. R. B. Lister, An explanation for the multivalued heat transport found experimentally for convection in a porous medium, Journal of Fluid Mechanics 214 (1990) 287–320.

[11] C. W. Horton, F. T. Rogers, Convection currents in a porous medium, Journal of Applied Physics 16 (1945) 367–370.

[12] E. R. Lapwood, Convection of a fluid in a porous medium, Proceedings of the Cambridge Philosophical Society 44 (1948) 508–521.

[13] W. Smith, F. G. Hammitt, Natural convection in a rectangular cavity with internal heat generation, Nuclear Science and Engineering 25 (1966) 328–342.

[14] H. Bhowmik, K. W. Tou, Experimental study of transient natural convection heat transfer from simulated electronic chips, Experimental Thermal and Fluid Science 29 (2005) 485–492.

[15] J. K. Lee, K. Y. Suh, K. J. Lee, J.-I. Yun, Experimental study of natural convection heat transfer in a volumetrically heated semicircular pool, Annals of Nuclear Energy 73 (2014) 432–440.

[16] B. Straughan, Stability and Wave Motion in Porous Media, Springer, New York, NY, 2008.

[17] A. Barletta, Routes to Absolute Instability in Porous Media, Springer, New York, NY, 2019.